

International Journal of Green Energy

ISSN: 1543-5075 (Print) 1543-5083 (Online) Journal homepage: www.tandfonline.com/journals/ljge20

Quantitative analysis and co-optimization of cathode catalyst layer compositions and operating conditions on cost and performance of PEM fuel cell

Xiongping Lin, Ruoyu Dai, Yiming Xu & Jieqing Zheng

To cite this article: Xiongping Lin, Ruoyu Dai, Yiming Xu & Jieqing Zheng (2024) Quantitative analysis and co-optimization of cathode catalyst layer compositions and operating conditions on cost and performance of PEM fuel cell, International Journal of Green Energy, 21:3, 651-665, DOI: 10.1080/15435075.2023.2204342

To link to this article: https://doi.org/10.1080/15435075.2023.2204342

Published online: 01 May 2023.

Submit your article to this journal

Article views: 249

View related articles

View Crossmark data

Citing articles: 2 View citing articles

Full Terms & Conditions of access and use can be found at
https://www.tandfonline.com/action/journalInformation?journalCode=ljge20

INTERNATIONAL JOURNAL OF GREEN ENERGY
2024, VOL. 21, NO. 3, 651–665
https://doi.org/10.1080/15435075.2023.2204342

Taylor & Francis
Taylor & Francis Group

Check for updates

Quantitative analysis and co-optimization of cathode catalyst layer compositions and operating conditions on cost and performance of PEM fuel cell

Xiongping Lin[a,b], Ruoyu Dai[b], Yiming Xu[b,c], and Jieqing Zheng[b]

[a]Chengyi College, Jimei University, Xiamen, Fujian, China; [b]Key Laboratory of Energy Cleaning Utilization and Development of Fujian Province, Jimei University, Xiamen, Fujian, China; [c]School of Automotive Studies, Tongji University, Shanghai, China

ABSTRACT

Increasing the net power density of proton exchange membrane fuel cell without extra cost is beneficial to its commercialization. To this end, a one-dimensional, two-phase, non-isothermal model was developed in this work. The influences of cathode catalyst layer compositions including the mass ratio of ionomer to carbon ($R_{i/c}$) and mass ratio of platinum to carbon ($R_{pt/c}$) and operating conditions including temperature, cathode relative humidity (RHc), anode relative humidity (RHa), and operating voltage (V) on the cost and performance of fuel cell were quantitatively investigated by range and variance analyses based on an orthogonal test. The results indicate that $R_{i/c}$ is the most significant factor affecting net power and unit power price. In addition, the RHc and V are also sensitive parameters to the net power, while $R_{pt/c}$ affects the unit power price. Finally, with the consideration of the interaction between the operating conditions and the cathode catalyst layer compositions, a multi-objective optimization was conducted to improve the aforementioned two indicators. Compared to the base case, the optimized fuel cell achieves a net power increase of 50.8% and a 24.7% reduction in unit power price, which allows the realization of a high-performance, low-cost fuel cell.

ARTICLE HISTORY
Received 5 December 2022
Accepted 14 April 2023

KEYWORDS
PEMFC; cathode catalyst layer compositions; operating conditions; quantitative analysis; multi-objective optimization

1. Introduction

In the past few decades, a stronger need to utilize renewable energy to replace conventional fossil fuels to slow down climate change has arisen (Rivarolo et al. 2020; Cai et al. 2022). Proton exchange membrane fuel cells (PEMFCs) are considered as one of the most promising energy utilization technologies due to its high energy efficiency, zero-emissions nature, *etc* (Jiao et al. 2021; Zhao et al. 2021). Currently, the large-scale commercialization of PEMFCs is still hindered by performance, cost, and durability issues. There are many factors affecting the development of fuel cell technology, such as the structure of components (Badduri et al. 2019; Yang et al. 2021; Zhang et al. 2022), materials (Chen et al. 2021; Iskandarani et al. 2022; Song et al. 2019; Wang et al. 2019), and operating conditions (Ogungbemi et al. 2020; Huo et al. et al. 2021; Zhang et al. 2018). Hence, searching for the optimal parameters to satisfy the requirement of PEMFC commercialization becomes vital for researchers.

There have been numerous studies concerning the output performance of PEMFCs by optimizing the operating conditions. To increase the water recovery efficiency and improve the performance of PEMFCs, multi-objective optimization was performed by combining the CFD model and NSGA-II algorithm (Yao et al. 2022). The result indicated that adjusting the humidification temperature and relative humidity (RH) at the cathode inlet rationally, and keeping the operating temperature moderately contribute to the balance between the electrochemical and water recovery performances. Su et al. (2022) developed an artificial neural network (ANN) model to predict the voltage distributions of a 60-kW stack under different operating pressures and load currents. Nanadegani *et al.* (Nanadegani et al. 2020). also used the ANN method to investigate the effects of temperature, RH in the cathode and anode, and stoichiometry on the cathode and anode sides on the power output of a PEMFC. Huanget et al. (2022) integrated a neural network method with a meta-heuristic algorithm based on the open-cathode PEMFC combined with ultra-thin vapor chambers. As a result, they identified the optimal fan power and maximum electrical efficiency of the stack with various currents. Ghasabehi et al. (2021). combined the response surface method with Non-dominated Sorting Genetic Algorithm ii (NSGA ii) to select the voltage and maximum power density under various operating conditions, such as the amount of reactant gas, operating temperature, pressure, and RH. To explore the range of ideal operating conditions efficiently, a semi-empirical fuel cell stack model was coupled with an associated balance of plant model (Wishart, Dong, and Secanell 2006). Its purpose was also to maximize the net system power and exergetic efficiency.

Except for the operating conditions, the optimization regarding the catalyst layer composition has been discussed extensively. Since the cathode catalyst layer (CCL) is the main place where sluggish oxygen reduction reaction occurs and most heat is released, numerous researchers focus on the optimization of CCL compositions, such as Pt loading or ionomer content. Wang et al. (2020) found the best optimal parameters for the catalyst layer composition by combining

CONTACT Yiming Xu xymdoc@tongji.edu.cn; Jieqing Zheng zhengjieqing@jmu.edu.cn b Key Laboratory of Energy Cleaning Utilization and Development of Fujian Province, Jimei University, Xiamen, Fujian, 361021, Chinac School of Automotive Studies, Tongji University (Jiading Campus), Shanghai 201804, China

© 2023 Taylor & Francis Group, LLC

a data-driven surrogate model and a stochastic optimization algorithm, which consequently improved the maximum power density of PEMFCs. Ebrahimi et al. (2016) determined the optimum catalyst loading distribution along the CCL via a novel algorithm based on the numerical model and the Nelder-Mead simplex optimization method. As a result, the maximum PEMFC density is increased by about 7%. To achieve the desired temperature uniformity of the CCL and power density of PEMFCs, Xu et al. (2022) developed a 1-d PEMFC model and attained the ideal ionomer-gradient distribution across the CCL with three sub-layers via a combination of NSGA-II and TOPSIS. Similarly, Fan et al. (2023) investigated the effects of operating voltage and the gradients of platinum and ionomer across the CCL thickness on output performance and current density distribution. After a multi-objective optimization via NSGA-II and a Pareto optimal solution, the current density uniformity and the output performance were improved by 71.4% and 5.26%, respectively. The desired current density uniformity and the best power density of PEMFCs were also maintained by optimizing graded-catalyst loading along the gas channel (Zhang et al. 2015). Besides, Ebrahimi et al. (2017) integrated a computational fluid dynamic model and genetic algorithm optimization method to find the best Pt loading distribution along the channel. The Pt loading was assumed to follow a polynomial function with unknown coefficients. After estimating the unknown coefficients, the maximum PEMFC power density can be increased by about 14%.

According to the aforementioned literature, much research effort has been applied in the search for the ideal operating conditions or distributions of CCL compositions. Wang et al. (2020) have also discussed the applications and potential of the Machine learning and artificial intelligence in the development of performance prediction, material selection, structure design and optimization, and so on. However, the physio-chemical process in PEMFCs is a combination of operating conditions and CCL composition. Jiang et al. (2018) used the elementary effect method based on Monte Carlo experiments to analyze the total 22 uncertain parameters (including geometric, physical and electrochemical parameters). The effects of each parameter on the PEMFC performance were investigated and the sensitivity analysis was also conducted. Furthermore, there are mutual effects between the operating conditions and CCL composition. For example, Alink et al. (2020) found the optimum ionomer content is dependent on the operating load and gas RH via a full parametric study of various catalyst layer compositions, while the proton conductivity is affected by the ionomer content, which in turn influences the voltage. Similarly, Secanell et al. (2007) concluded that the optimal catalyst layer composition and gas diffusion layer (GDL) porosity are directly correlated with the operating conditions. However, multi-variable optimization involving the operating conditions as well as CCL constituents is still rarely discussed. Since the key roles of the operating conditions and CCL compositions in PEMFCs, it is practical to employ multi-variable optimization to search for the optimal combination. Hence, it is worth identifying the ideal operating conditions and CCL compositions via the multi-variable optimization due to the interactions between them.

Additionally, the aforementioned studies mainly focus on the output performance or energy efficiency of a PEMFC. In fact, these objectives are the most common in current research, which cannot fully reflect the comprehensive performance of PEMFCs. As for the CCL composition, components such as Pt and ionomer elements of the device, not only exert essential influences on the reaction rate, mass transfer, and degradation (Okonkwo et al. 2021; Okonkwo 2021; Prokop, Drakselova, and Bouzek 2020) but also account for almost half of the overall PEMFC cost (Muzaffar, Kadyk, and Eikerling 2018; Shahgaldi et al. 2018; Stariha et al. 2016). Similarly, the operating conditions (temperature, gas pressure, *etc.*) could consume extra power or heat. Therefore, the cost caused by these factors is also a key issue for PEMFC commercialization. Srinivasarao et al. (2011) identified the design parameters of a CCL with the goal of maximizing current generation per unit Pt loading and minimizing the cost of the catalyst layer, but almost all operating conditions are kept constant except for the voltage. Kazeminasab et al. (2015) selected the Pt loading, ionomer content, agglomerate radius, porosity, and water saturation in CCL as the decision variables and found the best trade-off between the cost and the performance of the CCL at 0.6 V. The main operating conditions were also unchanged in the study. Recently, the 4Es (energy, exergy, economy, and environment) have received attention (Xie et al. 2022; Zhao et al. 2021). Zhao et al. (2021) conducted a multi-objective optimization of the 4Es based on the combination of PEMFCs, cooling, heating, and a power system. As a result, the suitable operating conditions of PEMFCs and refrigeration system were identified after optimization, but the effects of CCL compositions were not their primary focus. In a word, advancements in materials, operational control, and design are crucially important to cost reduction and performance enhancement (Ding et al. 2022; Wang et al. 2020). Currently, little attention is paid to finding a more cost-effective PEMFC with a high-performance level via considering the operating conditions and CCL compositions simultaneously.

Moreover, there are different influences caused by various factors in terms of operating conditions or CCL compositions. Wang et al. (2019) found that the most important factor affecting the PEMFC performance is the air stoichiometric ratio by orthogonal test method while the effect of anode RH is minimal. The importance of co-flow or counter-flow configurations and cathode operating parameters with respect to the stack power density and efficiency was also conducted based on the orthogonal method (Lin et al. 2019). As a result, the optimum power density and system efficiency correspond to different stack configurations and operating conditions. To evaluate the effects of seven operating parameters on the PEMFC output performance and internal gas concentration distribution quantitatively, Chen et al. (2019) established a 3-d PEMFC model to investigate and calculate the influential proportion of each operating parameter and estimate its effects. Elsewhere, the sensitivities of several operating parameters to current density and internal gas distribution were also obtained based on the response surface methodology (Jin et al. 2021). The finding indicated that the operating pressure has the most significant effect on both

current density and gas distribution. Besides, Li et al. (2022) evaluated the sensitivities of the CCL design parameters to PEMFC performance and oxygen distribution with a cross-dimensional PEMFC agglomerate model. They found that the sensitivities of the design parameters (Pt radius, carbon radius, Pt loading, *etc.*) evolve with the increase of the current density. The influences of operating parameters and CCL composition have been investigated elsewhere, but the sensitivities of these relevant parameters including both the operating parameters and CCL compositions remain to be discovered. Since the operating conditions and CCL compositions affect each other, it is unclear which parameter plays a key role in determining the output performance and cost of the PEMFC.

Over all, searching for the best combination of the operating conditions and CCL compositions from the perspective of the PEMFC performance and cost is essential for the large-scale commercialization of PEMFC. Besides, identifying the parameters of the operating conditions and CCL compositions that have the greatest impact on the PEMFC performance and cost is of practical significance, as it would offer specific and effective references for the future design of a PEMFC. To achieve these goals outlined, a one-dimensional, two-phase, non-isothermal finite-difference model accounting for agglomerated catalyst and ionomer swelling was developed under the MATLAB™ environment. Based on orthogonal tests, the influences of CCL composition and operating conditions on the cost and performance of PEMFCs were quantitatively investigated by range and variance analyses. Finally, the multi-objective optimization based on the non-dominated sorting genetic algorithm (NSGA-II) was applied to analyze the best operating conditions and CCL composition to improve the net power and reduce the unit power price.

2. Model development

2.1. Computational domain and governing equations

The one-dimensional model is limited in an MEA considering the through-plane (TP) direction which is perpendicular to the PEM, corresponding to the x-axis in Figure 1. The heights of GDL, MPL, and PEM are 190, 30, and 18 μm, respectively. The anode catalyst layer is 6 μm while the CCL is 8 μm. A series of conservation equations used in the non-isothermal, two-phase model are listed in Table 1 and the related source terms are

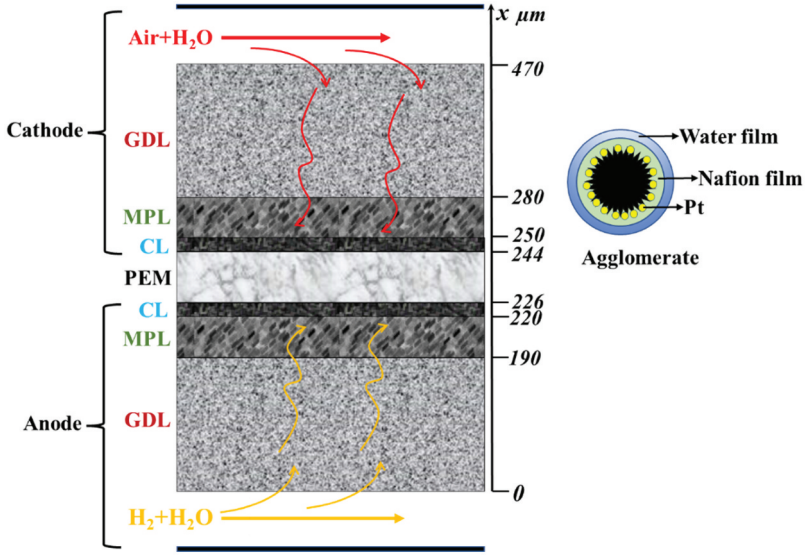

Figure 1. PEMFC structure and computational domain.

Table 1. Governing equations.

Description	Conservation equation
Gas	$\cdot(\rho_g \vec{u}_g) = S_m$
Gas species	$\cdot(C_g x_i \vec{u}_g) = \quad \cdot(C_g D_i^{eff} \quad x_i) + S_i$
Energy	$\cdot(\varepsilon s \rho_l c_{p,l} \vec{u}_l T + \varepsilon(1-s)\rho_g c_{p,g} \vec{u}_g T) = \quad \cdot(k \quad T) + S_T$
Liquid saturation	$- \quad \cdot\left(\frac{\rho_l}{M_{H_2O}} \frac{K_l}{\mu_l} \frac{dP_c}{ds} \quad s\right) = S_s$
Dissolved water	$\cdot\left(\frac{i}{F} n_d\right) + \quad \cdot(D_T \quad T) = \quad \cdot\left(\frac{\rho_m}{EW} D_\lambda \quad \lambda\right) + S_d$
Charges	$\begin{cases} \cdot(-\sigma_e \quad \phi_e) = S_e GDLs + MPLs + CLs \\ \cdot\left(-\sigma_p \quad \phi_p\right) = S_p CLs + MEM \end{cases}$
Darcy's equation	$\vec{u}_g = -\frac{K_g}{\mu_g} \quad P_g$

listed in Table 2. For the sake of simplicity, the relevant structure parameters, and transport correlations of this model are given in Table 3 to close the governing equations. Other detailed model information can be found elsewhere (Xu et al. 2023). Several main assumptions are made when solving these equations:

(1) All gas species follow the ideal gas law (Xing et al. 2014; Zhang and Jiao 2018);
(2) The gas and liquid two-phase flow is laminar due to the low velocity (Zhang and Jiao 2018; Zhang et al. 2018);
(3) The GDLs, MPLs, and CLs are treated as isotropic (Chen et al. 2018; Pasaogullari and Wang 2005);
(4) Water produced is assumed to be in dissolved form due to the ionomer film covering the Pt particle (Moein-Jahromi Kermani 2021; Xing et al. 2014);
(5) The PEMFC is operated in steady state conditions;

Table 2. Source terms.

Term	Expression
S_m	$S_{H_2} + S_{O_2} + S_{H_2O}$
S_{H_2}	$\begin{cases} -\frac{i}{2F} & aCL \\ 0 & others \end{cases}$
S_{O_2}	$\begin{cases} -\frac{i}{4F} & cCL \\ 0 & others \end{cases}$
S_{H_2O}	$\begin{cases} -S_{vl} & GDLs + MPLs \\ -S_{vl} - S_{vd} & CLs \end{cases}$
S_T	$\begin{cases} H_{ec}S_{vl} + \sigma_e \lVert \nabla \phi_e \rVert^2 & GDLs + MPLs \\ H_{ec}(S_{vl} + S_{vd}) + \sigma_e \lVert \nabla \phi_e \rVert^2 + \sigma_p \lVert \nabla \phi_p \rVert^2 + J_a\lvert\eta_a\rvert - \frac{J_a \Delta S_{HOR} T}{2F} & ACL \\ H_{ec}(S_{vl} + S_{vd}) + \sigma_e \lVert \nabla \phi_e \rVert^2 + \sigma_p \lVert \nabla \phi_p \rVert^2 + J_c\lvert\eta_c\rvert - \frac{J_c \Delta S_{ORR} T}{2F} & CCL \\ \sigma_p \lVert \nabla \phi_p \rVert^2 & PEM \end{cases}$
S_{vl}	$\begin{cases} \gamma_{con}\varepsilon(1-s)(C_v - C_{sat}), C_v \geq C_{sat} \\ \gamma_{eva}\varepsilon s(C_v - C_{sat}), C_v < C_{sat} \end{cases}$
S_d	$\gamma_d \frac{\rho_m}{EW}(\lambda_{eq} - \lambda)$
S_p	$\begin{cases} J_a, aCL \\ -J_c, cCL \end{cases}$
S_e	$\begin{cases} -J_a, aCL \\ J_c, cCL \end{cases}$

Table 3. Physical parameters and transport properties.

Parameter, unit	Correlation
MEM	$EW = 0.968$ kg mol^{-1}, $\rho_m = 1820$ kg m^{-3}
	$k_{PEM} = 0.177 + 3.7e^{-3}\lambda$ W m^{-1} K^{-1} (Burheim et al. 2010)
CL	$m_{Pt,a} = 0.1$, $m_{Pt,c} = 0.35$ mg cm^{-2}
	$K_{CL} = 1.0 \times 10^{-13}$ m^2, $\sigma_{CL} = 350$ S m^{-1}
MPL	$\varepsilon_{MPL} = 0.4$, $K_{MPL} = 1.0 \times 10^{-12}$ m^2
	$k_{MPL} = 0.534 + 0.4788s$W m^{-1} K^{-1} (Burheim et al. 2011)
	$\sigma_{MPL} = 1250$ S m^{-1}
GDL	$\varepsilon_{GDL} = 0.76$, $\delta_{GDL} = 190.0$ μm
	$k_{GDL} = 0.534 + 0.4788s$ W m^{-1} K^{-1} (Burheim et al. 2011)
	$K_{GDL} = 6.15 \times 10^{-12}$ m^2, $\sigma_{GDL} = 1250$ S m^{-1}
O_2 diffusion in water, m^2 s^{-1}	$D_{O_2,W} = 6.7 \times 10^{-9}$
O_2 diffusion in electrolyte, m^2 s^{-1}	$D_{O_2,i} = 1.3926 \times 10^{-10}\lambda^{0.708} exp\left(\frac{T-273.15}{106.65}\right)$
	$- 1.6461 \times 10^{-10}\lambda^{0.708} + 5.2 \times 10^{-10}$
Dissolved water diffusivity, m^2 s^{-1}	$D_\lambda = \begin{cases} \varepsilon_i^{1.5} 3.1 \times 10^{-7}\lambda\left(e^{0.28\lambda} - 1\right)e^{-2346/T} 0 < \lambda < 3 \\ \varepsilon_i^{1.5} 4.17 \times 10^{-8}\lambda\left(161e^{-\lambda} + 1\right)e^{-2346/T} \lambda \geq 3 \end{cases}$
Thermal-osmotic coefficient, mol m^{-1} s^{-1} K^{-1}	$D_T = \varepsilon_i^{1.6} 1.66 \times 10^{-5}/M_{H_2O} e^{-2297/T}$
Effective gas diffusivity, m^2 s^{-1}	$D_i^{eff} = \varepsilon^{1.5}(1-s)^{1.5} D_{0,i}\left(\frac{T}{T_{ref}}\right)^{1.5}\left(\frac{P_{ref}}{P}\right)$
Knudsen diffusion, m^2 s^{-1}	$D_{kn,i} = \frac{2}{3}\left(\frac{8RT}{\pi M_i}\right)^{0.5} r_p$
Mix gas diffusivity, m^2 s^{-1}	$D_{mix,i}^{eff} = \left(\frac{1}{D_i^{eff}} + \frac{1}{D_{kn,i}}\right)^{-1}$
Vapor saturation pressure, Pa	$log_{10}^{\frac{P_{sat}}{101325}} = -2.1794 + 0.02953(T - 273.15) - 9.1837 \times 10^{-5}(T - 273.15)^2 + 1.4454 \times 10^{-7}(T - 273.15)^3$
Capillary pressure, Pa	$P_c = -0.00011e^{(-44.02(s-0.496))} + 278.3e^{(8.103(s-0.496))} - 191.8$
Proton conductivity, S m^{-1}	$\sigma_p = \varepsilon_i^{1.5}(0.5139\lambda - 0.326)e^{1268\left(\frac{1}{303} - \frac{1}{T}\right)}$
Equilibrium water content	$\lambda_{eq} = 0.043 + 17.81RH - 39.85RH^2 + 36.0RH^3$
Electro-osmotic drag coefficient	$n_d = 2.5\frac{\lambda}{22}$

(6) The membrane is impermeable for electrons and gases (Zhang and Jiao 2018; Zhang et al. 2018);
(7) The effect of gravity is neglected (Wang et al. 2021; Zhang et al. 2018);
(8) Thermal equilibrium exists among gas, liquid, and solid phases in the model (Wang et al. 2021);
(9) The carbon loading determines the CL thickness. Once the total carbon load is determined, the thickness of CL can be assumed invariable. The variations in Pt loading, ionomer content, and ionomer swelling only affect the porosity of the CL.

2.2. Agglomerate sub-model of CCL

In this work, the spherical agglomerate model is performed to simulate the real CL structure and predict the electrochemical reaction at the macroscopic scale (Li et al. 2018; Zhang et al. 2018). The agglomerates are assumed to be covered by ionomer and liquid water films, respectively. The anode and cathode reaction rates are calculated based on the Butler-Volmer equations and the relevant correlations of the CCL agglomerate sub-model are listed in Table 4.

2.3. Boundary conditions

The operating conditions (temperature, inlet gas pressure and RH, electric potential) are specified at the anode and cathode GC/GDL interfaces in Figure 1, respectively. The anode electric potential is zero ($\phi_{e,a} = 0$) while the cathode potential is the operating voltage ($\phi_{e,c} = U$). Also, the liquid water saturation at the GC/GDL interfaces is kept at 0.12 (Vetter and Ogungbemi et al. 2019; Zhou, Putz, and Secanell 2017). The mole fractions of hydrogen and oxygen at the GC/GDL interfaces are shown below:

$$x_{H_2,a} = 1 - \frac{P_{sat} RH_a}{P_a} \tag{1}$$

$$x_{O_2,c} = 0.21\left(1 - \frac{P_{sat} RH_c}{P_c}\right) \tag{2}$$

2.4. Numerical procedures and validation

The conservation equations of this non-isothermal, two-phase model are developed by the BVP function in MATLAB™ software. The absolute error is set to 10^{-8} to guarantee computational accuracy. As for the model validation, it is affected by many parameters in the simulation model (Xie et al. 2022). Thus, the model verification is no longer limited to polarization curves in several literature (Ma et al. 2021; Wang et al. 2018; Zhang et al. 2020). In the present work, the polarization curves and ohmic resistance from Ref (Xie et al. 2023) are selected to compare with the numerical results. It is noteworthy that the operating conditions of the simulation are consistent with the literature. The experimental polarization curve and ohmic impedance were attained via a fuel cell test station (G20 Greenlight Innovation) and an electrochemical workstation (Gamry Interface 5000E), respectively. The single PEMFC used in the experiment has an active area 23.2 cm^2 with an identical three-serpentine flow field in the anode and cathode. More details about the experimental equipment and measures can refer to the literature (Xu et al. 2021). From Figure 2, the numerical results well match the experimental data.

Table 4. Agglomerate sub-model.

Parameter, unit	Correlation
Pt/C particles volume fraction (ε_{PtC})	$\frac{m_{PtC}}{\delta_{CL}}\left(\frac{1}{\rho_{Pt}} + \frac{1-R_{PtC}}{R_{PtC}}\frac{1}{\rho_C}\right)$
Ionomer phases volume fraction (ε_i)	$\frac{\zeta_{I/C} m_{Pt}}{\delta_{CL}\rho_i}\left(\frac{1}{\zeta_{pt/C}} - 1\right)\left(1 + \frac{M_i \rho_i}{\rho_i EW}\lambda\right)$
Number of agglomerate particles (N_{agg})	$\frac{\varepsilon_{PtC}}{4\pi/3 r_{agg}^3\left(1-w_{i,agg}\right)}$
Ionomer film height (δ_i), m	$r_{agg}\left(\sqrt[3]{\frac{\varepsilon_i\left(1-w_{i,agg}\right)}{\varepsilon_{PtC}} - w_{i,agg} + 1} - 1\right)$
Water film height (δ_w), m	$\sqrt[3]{\left(r_{agg}+\delta_i\right)^3 + \frac{3s\varepsilon_{CL}}{4\pi N_{agg}}} - \left(r_{agg}+\delta_i\right)$
CL porosity (ε_{CL})	$1 - \varepsilon_{PtC} - \varepsilon_i$
Effective reaction surface area (A_{eff}), m^{-1}	$\frac{\varepsilon_{Pt} m_{Pt}}{\delta_{CL}} S$
Reaction surface area (S), $m^2\ kg^{-1}$	$\left(227.79R_{PtC}^3 - 158.57R_{PtC}^2 - 201.53R_{PtC} + 159.5\right)\times 10^3$
Ionomer agglomerate surface area ($a_{agg,i}$), m^{-1}	$\frac{3\varepsilon_{PtC}\varepsilon_{CL}}{r_{agg}^3\left(1-w_{i,agg}\right)}\left(r_{agg}+\delta_i\right)^2$
Liquid water agglomerate surface area ($a_{agg,w}$), m^{-1}	$\frac{3\varepsilon_{PtC}\varepsilon_{CL}}{r_{agg}^3\left(1-w_{i,agg}\right)}\left(r_{agg}+\delta_i+\delta_w\right)^2$
Reaction rate constant (k_c), s^{-1}	$\frac{i_c^{ref} A_{eff}}{4F(1-\varepsilon_{CL})C_{O_2}^{ref}}\left(e^{-2\alpha_c F\eta_c/R/T} - e^{2\alpha_c F\eta_c/R/T}\right)$
Thiele's modulus (φ)	$\frac{r_{agg}}{3}\left(\frac{k_c}{w_{i,agg}^{1.5} D_{O_2,i}}\right)^{0.5}$
Effectiveness factor (E_{agg})	$\frac{1}{\varphi}\left(\frac{1}{\tanh(3\varphi)} - \frac{1}{3\varphi}\right)$
Anode reaction rate (J_a), A m^{-3}	$(1-s) i_a^{ref} A_{eff}\left(\frac{P_{H_2}}{C_{H_2}^{ref} H_{H_2}}\right)^{0.5}\left(e^{2\alpha_a F\eta_a/R/T} - e^{-2\alpha_a F\eta_a/R/T}\right)$
Cathode reaction rate (J_c), A m^{-3}	$4F\left(\frac{P_{O_2}}{H_{O_2}}\right)\left(\frac{1}{E_{agg}k_c(1-\varepsilon_{CL})} + \frac{r_{agg}+\delta_i+\delta_w}{r_{agg}}\left(\frac{\delta_i}{a_{agg,i}D_{O_2,i}} + \frac{\delta_w}{a_{agg,w}D_{O_2,w}}\right)\right)^{-1}$

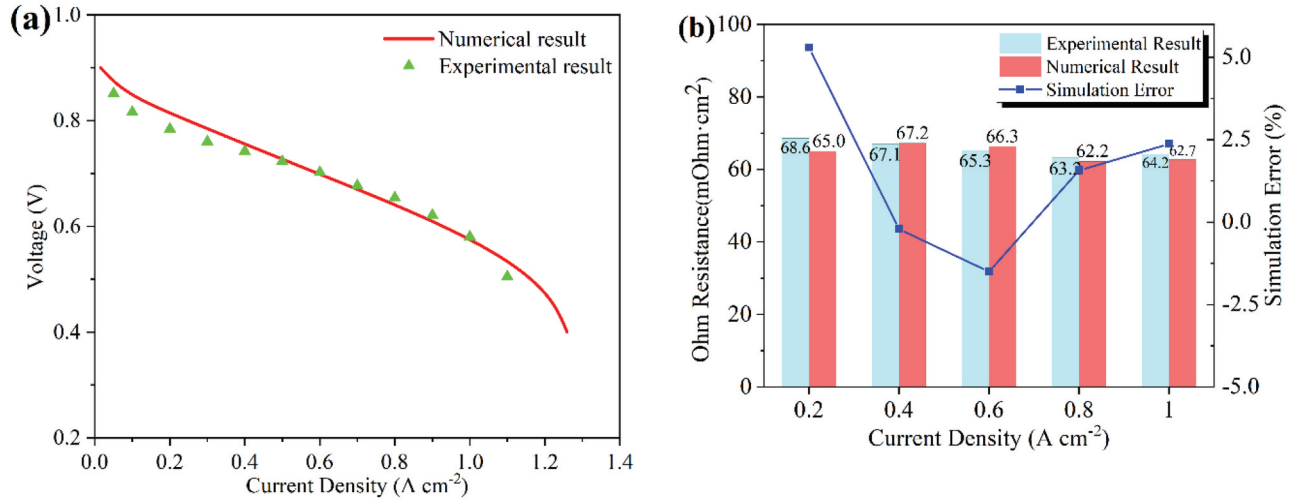

Figure 2. Comparison with measured data (RHa/RHc:50%, $T = 70$°C): (a) polarization curves (b) ohmic resistance.

Table 5. Constants used in the compressor model.

Constant	Value
Ambient temperature, T_e	298.15 K
Compressor efficiency, η_c	0.85
Mechanical efficiency, η_{mt}	0.85
Cathode supply air pressure, P	1 atm
Air excess ratio, λ_{air}	2.5

3. Optimization methods

3.1. Evaluation criteria for the fuel cell

Based on the PEMFC model described above, a multi-objective optimization approach is applied to optimize the performance of the PEMFC. There are two key evaluation criteria, namely the net power and unit power price. The net power can be described by the following equations (Ang et al. 2010; Xia et al. 2017).

$$W_N = IUA - W_{comp} - W_{others} \tag{3}$$

$$W_{comp} = \frac{C_p T_e}{\eta_c \eta_{mt}} \left[\left(\frac{P}{P_{in}} \right)^{0.286} - 1 \right] m_{air} \tag{4}$$

$$m_{air} = 3.57 \times 10^{-7} \lambda_{air} IA \tag{5}$$

$$W_{others} = 0.05IU \tag{6}$$

where W_N is the net power, W_{comp} is the power consumption of the compressor and W_{others} represents the other power loss. Some of the parameters in the above equations are assumed to be constants, while in practice they may vary with compressor size and full speed ratio. However, this does not affect the optimization procedure. The values of these constants are listed in Table 5.

Since the Pt/C and ionomer account for almost half of the overall PEMFC cost (Shahgaldi et al. 2018; Stariha et al. 2016), their total cost could be regarded as a good indicator of the cost of CL. Therefore another optimization indicator can be calculated as follows:

$$P_U = \frac{100 P_{Pt} m_{pt} A + 10 P_{In} \delta_{CL} A \rho_m \omega_i}{W_N} \tag{7}$$

where P_U denotes the unit power price, P_{Pt} is the price ($/g) of Pt and the value in this work is 30.29 (Xia et al. 2022). P_{Pt} represents the price of ionomer and is taken as 24.1 (Kazeminasab, Rowshanzamir, and Ghadamian 2015).

3.2. Identification of significant variables

The selection of decision variables in traditional optimization studies typically relies on experience, which suffers from an inevitable subjectivity. To identify significant variables before optimization, this study uses range and variance analyses to clarify the degree of influence of each variable on fuel cell performance. Range analysis is a statistical technique used to determine the sensitivity of parameters based on the results of orthogonal tests. The distance between the extreme values of the data is used to define the range. The larger the range, the greater the effect (Wang et al. 2019). The range analysis is given by:

$$R_X = \max\{K_{Xi}\} - min\{K_{Xi}\} \tag{8}$$

where R_X is the range of factor X; K_{Xi} denotes the average value of the orthogonal tests which contain the factor X in level i.

The advantages of range analysis are that it is simple, intuitive, and easy to understand. It should be noted, however, that range analysis cannot distinguish between data fluctuations caused by changes in test conditions and those arising from test errors. In addition, range analysis cannot provide an accurate quantitative analysis of the significance of the factors. Hence, a variance analysis is essential for estimating the credibility of range analysis and identifying the factors with statistical significance. The calculation process of variance analysis can be described as follows:

Table 6. Six parameters and their selected levels.

No.	Parameter	Abbreviation	Level 1	Level 2	Level 3	Level 4
1	Operating temperature (K)	T	343.15	348.15	353.15	363.15
2	Anode RH (-)	RH_a	0.5	0.6	0.7	0.9
3	Cathode RH (-)	RHc	0.5	0.6	0.7	0.9
4	Operating voltage (V)	U	0.4	0.5	0.6	0.7
5	Mass ratio of ionomer to carbon (-)	R_{ic}	0.4	0.8	1.2	1.6
6	Pt loading (mg cm^{-2})	M_{pt}	0.1	0.3	0.5	0.8

$$SS_T = SS_{factor} + SS_{error} \tag{9}$$

$$df_T = df_{factor} + df_{error} \tag{10}$$

$$MS_{factor} = \frac{SS_{factor}}{df_{factor}} \tag{11}$$

$$MS_{error} = \frac{SS_{error}}{df_{error}} \tag{12}$$

where SS_T, SS_{factor}, and SS_{error} are the sum of squares (SS) for the total, each factor, and the error, respectively; df_T, df_{factor}, and df_{error} denote the total degrees of freedom (DOF) for the total, each factor, and the error, respectively; MS_{factor} and MS_{error} represent the mean square (MS) of each factor and error. The F-value for each factor (F_{factor}) can then be obtained according to Eq. (13):

$$F_{factor} = \frac{MS_{factor}}{MS_{error}} \tag{13}$$

The critical value of F (F_{critical}) is a function of the DOF of the numerator and the denominator and the significance level. If $F_{factor} > F_{\text{critical}}$, this factor can be considered to exert a significant influence on the test results.

The orthogonal numerical test is an effective analysis method for the multiple influential factors based on probability theory and mathematical statistics. As mentioned before, both range analysis and variance analysis should be conducted based on the results of orthogonal tests. In this paper, the operating conditions including temperature (T), anode humidity (RH_a), cathode humidity (RH_c), voltage (V), and CCL composition parameters including platinum loading (M_{pt}) and mass ratio of ionomer to carbon (R_{ic}) are selected as the influential factors. The values of factors and levels are listed in Table 6. According to the factors and corresponding levels, the orthogonal numerical test table L28 (3^6) in Table 2 is designed. To evaluate each

Table 7. L28 (3^6) orthogonal design table and its results.

	Factors						Results	
No.	T	RH_a	RH_c	U	R_{ic}	M_{pt}	NP	UPP
1	353.15	0.5	0.7	0.7	1.2	0.3	9.2	74.1
2	353.15	0.7	0.9	0.6	0.4	0.5	13.3	52.3
3	363.15	0.7	0.7	0.4	0.8	0.3	10.1	61.2
4	363.15	0.5	0.9	0.5	1.6	0.5	6.2	143.7
5	343.15	0.5	0.5	0.4	0.4	0.1	11.2	36.7
6	348.15	0.9	0.7	0.6	1.2	0.1	11.7	46.0
7	343.15	0.7	0.6	0.5	1.2	0.7	13.8	70.2
8	363.15	0.9	0.7	0.7	1.6	0.7	8.5	121.1
9	348.15	0.5	0.6	0.6	0.8	0.7	12.0	75.2
10	353.15	0.5	0.5	0.5	0.8	0.7	13.2	68.1
11	343.15	0.9	0.9	0.4	1.6	0.7	7.9	129.6
12	343.15	0.7	0.9	0.7	0.8	0.3	11.7	52.9
13	353.15	0.9	0.9	0.5	1.2	0.1	8.8	60.9
14	343.15	0.5	0.7	0.6	1.6	0.5	11.0	80.3
15	363.15	0.5	0.6	0.7	0.4	0.1	6.0	68.5
16	343.15	0.6	0.5	0.7	1.2	0.5	9.0	91.2
17	363.15	0.7	0.5	0.6	1.2	0.7	11.6	83.2
18	363.15	0.9	0.5	0.5	0.4	0.3	14.5	38.1
19	348.15	0.7	0.7	0.5	0.4	0.5	14.2	49.0
20	353.15	0.6	0.7	0.4	0.4	0.7	14.1	59.5
21	353.15	0.6	0.5	0.6	1.6	0.3	9.6	77.3
22	363.15	0.6	0.9	0.6	0.8	0.1	10.8	44.1
23	348.15	0.5	0.9	0.4	1.2	0.3	8.5	80.0
24	348.15	0.6	0.9	0.7	0.4	0.7	8.6	97.5
25	353.15	0.9	0.6	0.7	0.8	0.5	10.2	74.4
26	343.15	0.9	0.6	0.6	0.4	0.3	13.3	41.5
27	348.15	0.7	0.5	0.7	1.6	0.1	8.6	69.7
28	353.15	0.7	0.6	0.4	1.6	0.1	5.9	102.8
29	343.15	0.6	0.7	0.5	0.8	0.1	13.5	35.3
30	348.15	0.9	0.5	0.4	0.8	0.5	14.0	54.1
31	363.15	0.6	0.6	0.4	1.2	0.5	8.1	101.8
32	348.15	0.6	0.6	0.5	1.6	0.3	8.7	85.5

group of combinations, the unit power price (*UPP*, $/kW) and net power (*NP*, kW) are obtained using the finite difference model (Table 7).

3.3. Multi-objective optimization algorithm

Previous analysis shows that it is difficult to find a globally optimal solution to achieve the maximum power density and the minimum cost per unit of power because these objects are mutually constrained and affect each other. The Pareto optimal bound is usually adopted to represent the best compromise between each decision variable. A non-dominated sorting genetic algorithm-II (NSGA-II) is employed to solve the multi-objective optimization problem with the following genetic algorithm parameters: population size of 100, maximum evolutionary algebra of 200, and optimal individual coefficient of 0.3. The structure of the coupling algorithm is shown in Figure 3b. The objective function and constraints are written as follows:

$$\min\{-NP, UPP\} \tag{14}$$

$$\text{t.}\begin{cases} 343.15 \le T \le 363.15 \\ 0.5 \le \text{RHa} \le 0.9 \\ 0.5 \le \text{RHc} \le 0.9 \\ 0.4 \le \text{U} \le 0.7 \\ 0.4 \le \text{Ric} \le 1.6 \\ 0.1 \le \text{Mpt} \le 0.8 \end{cases} \tag{15}$$

4. Results and discussion

4.1. Range analysis

Based on Table 4, the range analysis is carried out in this subsection. Figure 4 represents the net power and unit power price range values. The factors with larger range values are considered more important. The importance of six factors on net power is (in descending order) as follows: R_{ic}, *U*, *RHc*, *T*, M_{pt}, and *RHa*. The unit power price is affected by the following factors: R_{ic}, M_{pt}, *U*, *RHc*, *T*, and *RHa*.

Figure 5 shows the variation in net power and unit power price with the levels of different factors. In Figure 5(a), the net power decreased from 11.5 kW to 9.5 kW when *T* increased

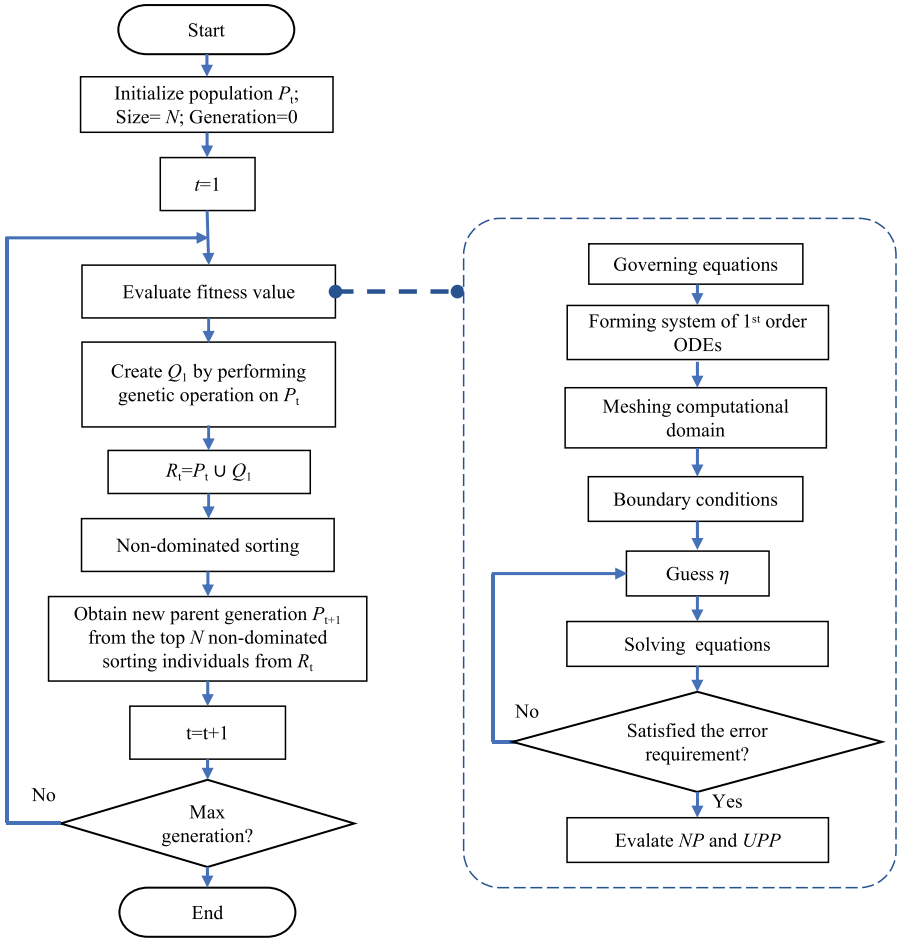

Figure 3. Flow-chart through the bvp4c-NSGA II algorithm.

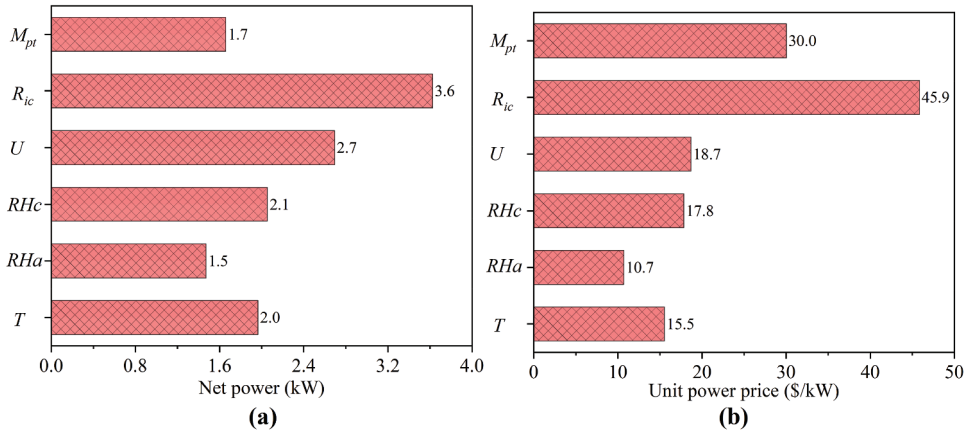

Figure 4. Range values of different factors in the (a) net power and (b) unit power price.

from 343.15 K to 363.15 K. This can be attributed to the exponential relationship between temperature and saturated water vapor pressure, the higher the temperature, the more significant the dilution effect on the reaction gas at the same RH, the lower the oxygen molar fraction, and therefore the net power of the cell is reduced. Meanwhile, the unit price increases from 67.2 $/kW to 82.7 $/kW when the temperature increases from 343.15 K to 363.15 K due to the decrease in the net power of the fuel cell. Hence, the optimal temperature is 343.15 K.

The effect of RH_a on the net power of the fuel cell is shown in Figure 5(b). RH_a is increased from 0.5 to 0.7, and the net power is improved from 9.6 kW to 11.3 kW. This is caused by the increase in anode humidity which reduces the membrane resistance. Consequently, the increase in anode humidity leads to a decrease in the unit power price from 78.3 $/kW to 67.4 $/kW. However, as the anode humidity continues to rise, the net power decreases. However, when the anode humidity reaches 0.7, the excessively high humidity reduces the partial pressure of hydrogen, the net power decreases and the unit power price increases as the anode humidity increases. Hence, 0.7 can be considered to be the optimum anode humidity.

Different from the anode humidity, the increase in cathode humidity increases the hydration of the membrane but dilutes the oxygen. PEMFC performance depends heavily on the trade-off between ohmic internal resistance and oxygen concentration. The trade-off results vary depending on the catalyst layer compositions and operating conditions. Hence, as shown in Figure 5(c) the impact of RHc does not seem to have a stable pattern when averaged over multiple factors. Hence, the influence of RH_c does not seem to have a stable pattern as shown in Figure 5(c). The maximum net power (11.5 kW) and the minimum unit power price (64.8 $/kW) are obtained at RH_c = 0.5. Figure 5(d) illustrates the variations in net power and unit power price with operating voltage. As the voltage increases, the net power shows a trend of first increasing, then decreasing. Similar phenomena have been reported in related studies (Fan et al. 2023), which are mainly due to the characteristics of the fuel cell. This also results in a price that varies with voltage, showing the opposite trend to net power. When U = 0.6 V, the fuel cell reaches its maximum net power and minimum unit power price with values of 11.7 kW and 62.5 $/kW, respectively.

In Figure 5(e), as R_{ic} increases, the net power of the fuel cell first increases slightly, then decreases significantly. A study by Wang et al. (2020) reported the same trend. This is because the increase of ionomer content leads to an enhancement of proton conduction but also makes oxygen transport difficult. Therefore, the performance of fuel cells depends on which factor plays a dominant role; when R_{ic} = 0.8, the net power density reaches a maximum of 11.9 kW. Furthermore, an increase in R_{ic} results in a higher cost for the catalyst layer and therefore leads to a higher unit power price. Thus, the lowest unit power price of 55.4 $/kW is obtained when R_{ic} = 0.4.

Similarly, an increase in Pt loading increases the cost of the catalyst layer, so in Figure 5(f), the lowest unit power price (58 $/kW) arises at M_{pt} = 0.1 mg cm^{-2}. It should be noted that an increase in Pt loading causes an increase in the electrochemical reaction area, as well as a decrease in reaction resistance, increasing net power. Hence, in Figure 5(f), when M_{pt} = 0.8 mg cm^{-2}, the net power reaches a maximum of 11.2 kW.

4.2. Variance analysis

As mentioned previously, the range analysis can identify the order of influence among factors and determine the optimal value of each factor, however, it is restricted to analyzing the influence of test error (E) and cannot quantify the contributions of each factor on the results. Thus, the application of variance analysis is necessary. The variance analysis is conducted based on the results of the previous calculations.

The results of T, RH_a, RHc, U, R_{ic}, and M_{pt} are given in Table 8. The F_{factor} values of U, R_{ic}, and M_{pt} exceed F_{critical} (α = 0.01) in net power, indicating these factors are significant. Similarly, R_{ic} and M_{pt} are significant factors in unit power price, due to their values exceeding F_{critical} (α = 0.01). Although the F_{factor} values of U and RHc are less than F_{critical} (α = 0.01) in unit power price, their values exceed F_{critical} (α = 0.05). Therefore, it is still considered that the effects of U and RHc on unit power price are significant. It should be noted that the SS values of T and RH_a are smaller than the SS values of

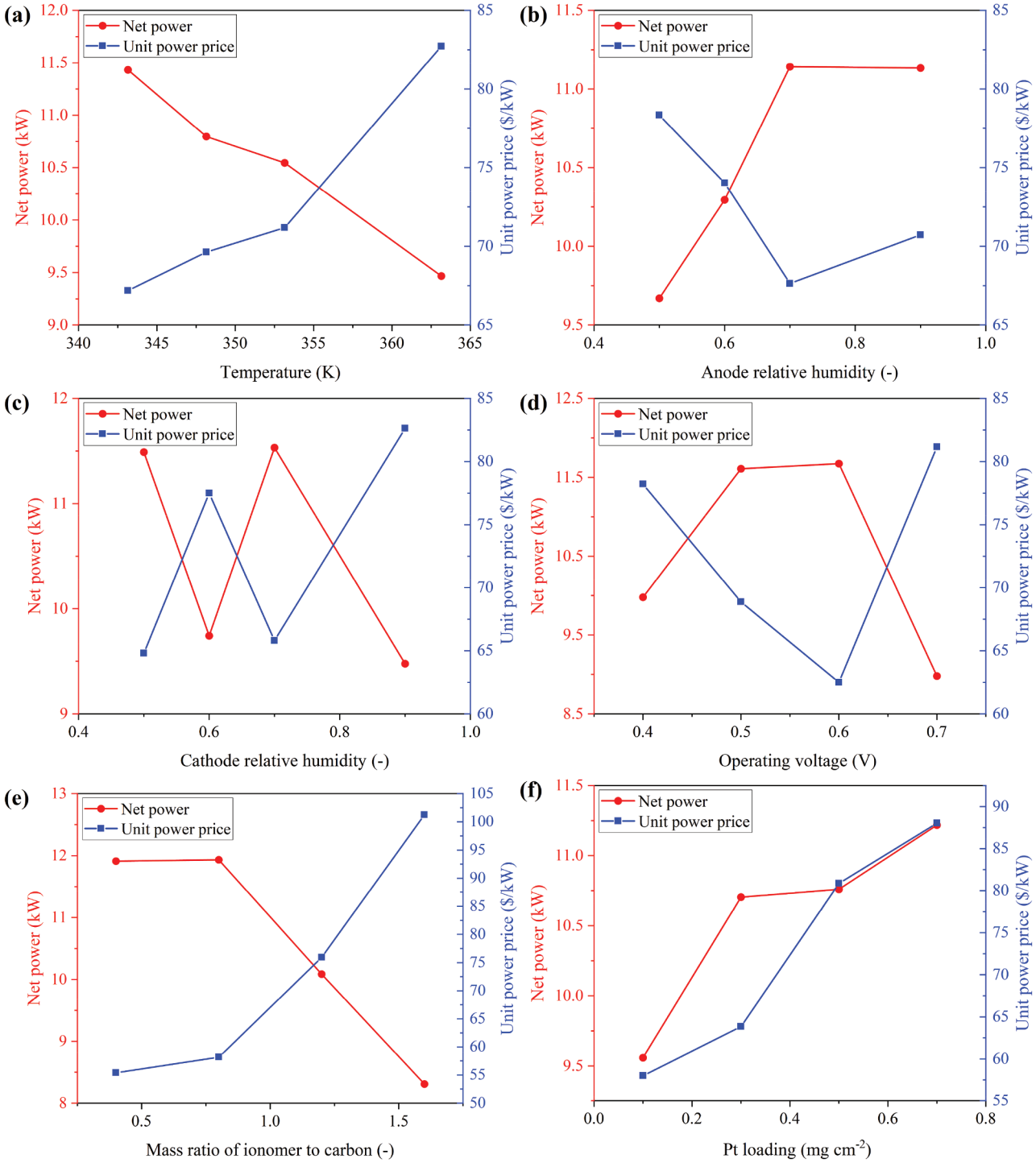

Figure 5. Effects of factors at different levels on the net power and unit power price: (a) temperature (b) anode relative humidity (c) cathode relative humidity (d) operating voltage (e) mass ratio of ionomer to carbon (f) Pt loading.

error in both net power and unit power price, indicating that the changes of T and RH_a have less impact on the orthogonal test results than even the error. Besides, in terms of net power, the SS value of M_{pt} is less than the SS value of error, and its F_{factor} value is smaller than F_{critical} ($\alpha = 0.05$). This indicates that changing the Pt loading has a negligible impact on fuel cell performance when the carbon loading is fixed. Therefore, considering the cost aspect, the Pt loading can be reduced appropriately.

Another purpose of variance analysis is to quantify the contributions of each factor to the results. Disregarding the effect of errors, the contributions of decision variables to the net power and unit power price are shown in Figure 6. The mass ratio of ionomer to carbon shows a significant influence both on the net power and unit power price, accounting for 39% and 52% of the total contribution, respectively. As mentioned previously, a sufficient ionomer content in CCL is conducive to enhanced proton transport, however, a higher ionomer content could

Table 8. The analysis of variance of net power and unit power price.

Index	Variable	SS	DOF	MS	F_{factor}	$F_{critical}$ (α = 0.05)	Significance (α = 0.05)	$F_{critical}$ (α= 0.01)	Significance (α= 0.01)
Net power	T	16.093	3	5.3645	3.31	3.41	N	5.74	N
	RH_a	12.231	3	4.077	2.51	3.41	N	5.74	N
	RHc	29.212	3	9.7372	6	3.41	Y	5.74	Y
	U	41.417	3	13.8058	8.51	3.41	Y	5.74	Y
	R_{ic}	72.084	3	24.0281	14.81	3.41	Y	5.74	Y
	M_{pt}	11.966	3	3.9887	2.46	3.41	N	5.74	N
	Error	21.088	13	1.6222					
	Total	204.092	31						
Unit power price	T	1139.4	3	379.79	3.02	3.41	N	5.74	N
	RH_a	503.5	3	167.83	1.34	3.41	N	5.74	N
	RHc	1851.4	3	617.13	4.91	3.41	Y	5.74	N
	U	1767.2	3	589.08	4.69	3.41	Y	5.74	N
	R_{ic}	10694.3	3	3564.78	28.38	3.41	Y	5.74	Y
	M_{pt}	4769.1	3	1589.71	12.66	3.41	Y	5.74	Y
	Error	1633	13	125.62					
	Total	22358	31						

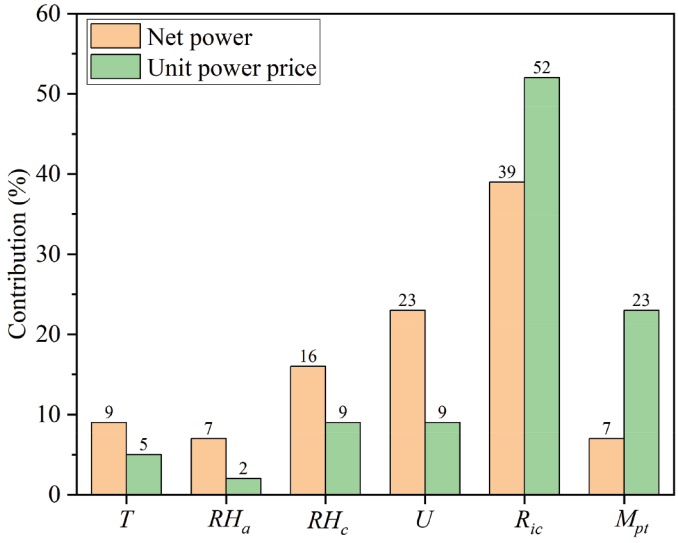

Figure 6. The contribution of decision variables to the net power and unit power price.

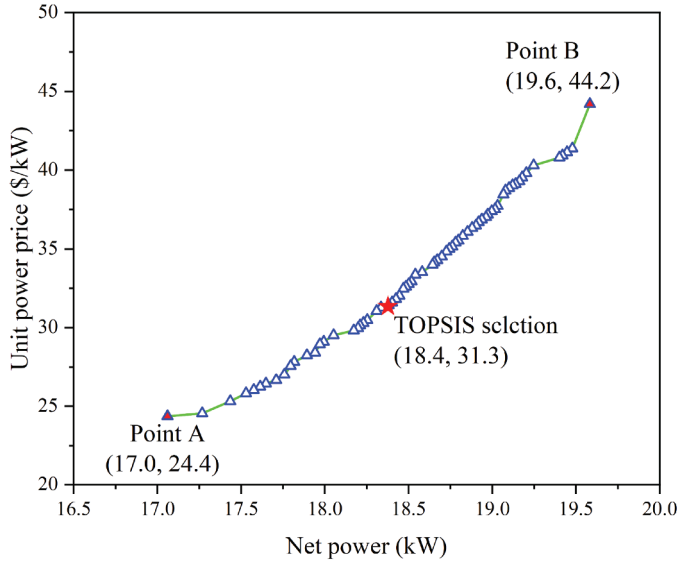

Figure 7. Pareto front of multi-objective optimization.

decrease the porosity of CCL and lead to a high mass diffusion resistance, thus deteriorating the performance of the cell. Moreover, a higher ionomer content increases the cost of PEM fuel cells. Therefore, it is quite feasible to optimize R_{ic} to improve fuel cell net power and the unit power price. In addition, among the factors affecting the net power of the fuel cell, the operating voltage and cathode humidity also occupy a large degree, the sum of which amounts to 39% of the total contribution. Therefore, for stationary fuel cell power plants, optimizing the operating voltage and cathode humidity is also an effective way in which to increase the net power. By optimizing only the fuel cell operating conditions, the increase in fuel cell net power will also cause a reduction in unit power price at the same total cost. The total contribution of temperature, cathode humidity, anode humidity, and operating voltage to the unit power price is also 25%, thus indicating the importance of optimizing the fuel cell operating conditions. It is worth noting that, in the optimization range selected in the present research, although Pt loadings account for 23% of the total unit power price contribution, its contribution to net power is only 7%. This indicates that optimization of ionomer content and operating conditions offers the possibility of achieving a low Pt content catalyst layer.

4.3. Multi-objective optimization results

Figure 7 depicts the Pareto optimal solution for optimizing net power and current density uniformity, indicating the conflict between the two objectives. The increase in net power ranging from 17.0 kW to 19.6 kW leads to a rise in unit power price from 24.4 $/kW to 44.2 $/kW. To validate the optimization results, three representative points A, B, and C are selected for comparisons with the base case. Points A and B are the endpoints of the Pareto front, and Point C is in the middle region of the Pareto front selected by the TOPSIS (Technique for Order of Preference by Similarity to Ideal Solution) method. Table 6 shows the comparison results of A, B, and C with the base model, and also listed the corresponding decision variables.

Table 9. Comparison of optimized result with the base model.

	Decision variable						Performance index	
Point	T	RH_a	RH_c	U	R_{ic}	M_{pt}	NP	UPP
A	343.15	0.9	0.9	0.50	0.43	0.10	17.0	24.4
B	343.15	0.9	0.9	0.53	0.68	0.68	19.6	44.2
C	343.15	0.9	0.9	0.51	0.56	0.29	18.4	31.3
Base	343.15	0.5	0.5	0.54	1.2	0.35	12.2	58.7

It can be observed from Table 9 that, Point A provides the solution with the lowest unit power price, however, this point is associated with the minimum net power. Conversely, Point B provides the maximum net power but the highest unit power price. Point B is the best solution for the case where power density is the main priority. It is worth noting that even at the lowest unit power price condition (Point A) in the Pareto front, the net power value is still much greater than the base case, meanwhile, at the maximum net power condition (Point B) the unit power price is also much smaller than the base case. Besides, the TOPSIS point is selected as the optimal case, compared to the base case, the fuel cell has a net power increase of 50.8% and a 24.7% reduction in unit power price. This evinces the effectiveness of multi-objective optimization.

5. Conclusion

A one-dimensional, two-phase, non-isothermal finite-difference model involving agglomerated catalyst and ionomer swelling was developed under the MATLAB™ environment. Thirty-two orthogonal tests with six factors including operating conditions and cathode catalyst layer composition and four levels were conducted. Then, the range and variance analyses were conducted. Finally, a multi-objective optimization was conducted considering the interaction between the operating conditions and the cathode catalyst layer composition. The following conclusions could be drawn:

(1) The range analysis on both cost and net power shows that the best levels of T, RH_a, RHc, U, and R_{ic} are 343.15 K, 0.7, 0.5, 0.6, and 0.4, respectively. The optimal value of M_{pt} is 0.8 mg cm^{-2} if considering only the net power, whereas the optimal value is 0.1 mg cm^{-2} when considering only the unit power price.
(2) The variance analysis confirms that U, R_{ic}, and RHc are the significant factors affecting the net power, while the unit power price are mostly controlled by R_{ic} and M_{pt}.
(3) In terms of the multi-objective optimization, three alternative results are provided: the maximum net power, the minimum unit power cost, and the optimum comprehensive performance. Compared to the base case, the optimized fuel cell has a net power increase of 50.8% and a 24.7% reduction in unit power price, which provides a solution capable of realizing high fuel cell performance at a low cost.

Nomenclature

A	Reaction surface area, m^{-1}
A_o	Catalyst surface area per unit mass, cm^2 g^{-1}
a	Water activity
C	Mole concentration, mol m^{-3}
c_p	Specific heat capacity, J kg^{-1} K^{-1}
D	Diffusivity, m^2 s^{-1}
F	Faraday constant, C mol^{-1}
H	Henry's constant, Pa m^3 mol^{-1}/ Phase change molar entropy, J mol^{-1}
i	Exchange current density, A m^{-2}
J	Volumetric current density, A m^{-3}
K	Permeability, m^2
k	Thermal conductivity, W m^{-1} K^{-1}/Swelling coefficient
Kc	Reaction rate constant
m	Mass loading, mg cm^{-2}
M	Molecular weight, kg mol^{-1}
n_d	Osmotic-drag coefficient
N	Number of agglomerates per unit volume of catalyst layer, m^{-3}
P	Pressure, Pa/Power density, W cm^{-2}
r	Radius, m
R	Universal gas constant, J mol^{-1} K^{-1}
s	Liquid water saturation
S	Source term/Reaction entropy, J mol^{-1} K^{-1}
T	Temperature, K
$\vec{v}$	Superficial velocity vector, m s^{-1}
Y	Mass fraction

Greek symbols

α	Transfer coefficient/Testing level
δ	Thickness, m
ε	Porosity/Volume fraction
η	Overpotential, V
λ	Membrane water content
μ	Dynamic viscosity, Pa s
ρ	Density, kg m^{-3}
σ	Electron/Proton conductivity, S m^{-1}
φ	Thiele's modulus
χ	Mole fraction
ϕ	Potential, V

Subscripts and Superscripts

a	Anode
ad	Absorption and desorption
agg	Agglomerate
C	Carbon
c	Cathode/Capillary
d	Osmotic-drag/Dissolved
e	Electron
ec	Evaporation and condensation
eff	Effective
eq	Equilibrium
g	Gas
i	Ionomer/i^{th} species
im	Immobile
in	Intrinsic
j	j^{th} species
kn	Knudsen diffusion
l	Liquid
p	Proton/Pore/Penetrated GDL
Pt	Platinum
r	Reaction
red	Reduced liquid water saturation
ref	Reference
sat	Saturation
vl	Vapor to liquid water
vd	Vapor to dissolved water
λ	Membrane water

Abbreviations

CL	Catalyst layer
GDL	Gas diffusion layer
HOR	Hydrogen oxidation reaction
CCL	Cathode catalyst layer
MEM	Membrane
MEA	Membrane electrode assembly
MPL	Micro-porous layer
HPR	High power density range
ORR	Oxygen reduction reaction
$PEMFC$	Proton exchange membrane fuel cell
$TOPSIS$	Technique for Order Preference by Similarity to an Ideal Solution

Acknowledgements

This work is supported by the National Natural Science Foundation of China (Grant No. 61871200), Natural Science Foundation of Fujian province, China (Grant No. 2021J10854) and Key Laboratory of Energy Cleaning Utilization and Development of Fujian Province (Jimei University) (No. JDNYKF202101).

Disclosure statement

No potential conflict of interest was reported by the authors.

Funding

The work was supported by the Fujian Provincial Department of Science and Technology [2021J10854]; Ministry of Science and Technology of the People's Republic of China [61871200]; Key Laboratory of Energy Cleaning Utilization and Development of Fujian Province [JDNYKF202101].

References

Alink, R., R. Singh, P. Schneider, K. Christmann, J. Schall, R. Keding, and N. Zamel. 2020. Full Parametric Study of the Influence of Ionomer Content, Catalyst Loading and Catalyst Type on Oxygen and Ion Transport in PEM Fuel Cell Catalyst Layers. *Molecules* 25 (7):1523. doi:10.3390/molecules25071523.

Ang, S. M. C., D. J. L. Brett, and E. S. Fraga. 2010. A multi-objective optimisation model for a general polymer electrolyte membrane fuel cell system. *Journal of Power Sources* 195 (9):2754–63. doi:10.1016/j.jpowsour.2009.10.095.

Badduri S R, G N Srinivasulu , G N S N RaoG et al. 2019. Experimental analysis of PEM fuel cell performance using lung channel design bipolar plate. *International Journal of Green Energy* 16 (15):1591–601. doi:10.1080/15435075.2019.1677238.

Burheim O S, J G Pharoah , H Lampert, P J.S Vie et al. 2011. Through-plane thermal conductivity of PEMFC porous transport layers. *Journal of Fuel Cell Science and Technology* 8 (2):1–11. doi:10.1115/1.4002403.

Burheim, O., P. J. S. Vie, J. G. Pharoah, and S. Kjelstrup. 2010. Ex situ measurements of through-plane thermal conductivities in a polymer electrolyte fuel cell. *Journal of Power Sources* 195 (1):249–56. doi:10.1016/j.jpowsour.2009.06.077.

Cai T, D. Zhao , S. H. Chan and M. Shahsavari Shahsavari. 2022. Tailoring reduced mechanisms for predicting flame propagation and ignition characteristics in ammonia and ammonia/hydrogen mixtures. *Energy* 260:125090. doi:10.1016/j.energy.2022.125090.

Chen, H., B Liu, T Zhang and Pei, P. 2019. Influencing sensitivities of critical operating parameters on PEMFC output performance and gas distribution quality under different electrical load conditions. *Applied Energy* 255:113849. doi:10.1016/j.apenergy.2019.113849.

Chen, H., X. Zhao, B. Qu, T. Zhang, P. Pei, and C. Li. 2018. An evaluation method of gas distribution quality in dynamic process of proton exchange membrane fuel cell. *Applied Energy* 232:26–35. doi:10.1016/j.apenergy.2018.09.031.

Chen, Q., Z Niu., H Li, K Jiao and Wang, Y. 2021. Recent progress of gas diffusion layer in proton exchange membrane fuel cell: Two-phase flow and material properties. *International Journal of Hydrogen Energy* 46 (12):8640–71. doi:10.1016/j.ijhydene.2020.12.076.

Ding, R., S. Zhang, Y. Chen, Rui, Z., Hua, K., Wu, Y., Li, X., Duan, X., Wang, X., Li, J. et al. 2022. Application of Machine Learning in Optimizing Proton Exchange Membrane Fuel Cells: A Review. *Energy and AI* 9:100170. doi:10.1016/j.egyai.2022.100170.

Ebrahimi, S., B. Ghorbani, and K. Vijayaraghavan. 2017. Optimization of catalyst distribution along PEMFC channel through a numerical two-phase model and genetic algorithm. *Renewable Energy* 113:846–54. doi:10.1016/j.renene.2017.06.067.

Ebrahimi, S., R. Roshandel, and K. Vijayaraghavan. 2016. Power density optimization of PEMFC cathode with non-uniform catalyst layer by Simplex method and numerical simulation. *International Journal of Hydrogen Energy* 41 (47):22260–73. doi:10.1016/j.ijhydene.2016.07.247.

Fan R, G Chang, Y Xu et al. 2023. Multi-objective optimization of graded catalyst layer to improve performance and current density uniformity of a PEMFC. *Energy* 262:125580. doi:10.1016/j.energy.2022.125580.

Ghasabehi, M., M. Shams, and H. Kanani. 2021. Multi-objective optimization of operating conditions of an enhanced parallel flow field proton exchange membrane fuel cell. *Energy Conversion and Management* 230:113798. doi:10.1016/j.enconman.2020.113798.

Huang, W., Q. Jian, S. Feng, and Z. Huang. 2022. A hybrid optimization strategy of electrical efficiency about cooling PEMFC combined with ultra-thin vapor chambers. *Energy Conversion and Management* 254:115301. doi:10.1016/j.enconman.2022.115301.

Huo S, Li L, Shi W et al. 2021. Characteristics of Cold Start Behavior of PEM Fuel Cell with Metal Foam as Cathode Flow Field under Subfreezing Temperature. *International Journal of Green Energy* 18 (11):1129–46. doi:10.1080/15435075.2021.1891911.

Iskandarani, B., R. Mojarrad, N. Yürüm A, S. Alkan Gürsel, and B. Yarar Kaplan. 2022. Electrospun Nanofiber Electrodes for Boosted Performance and Durability at Lower Humidity Operation of PEM Fuel Cells. *Energy & Fuels* 36 (16):9282–94. doi:10.1021/acs.energyfuels.2c01595.

Jiang, Y., Z. Yang, K. JIAO, and Q. Du. 2018. Sensitivity analysis of uncertain parameters based on an improved proton exchange membrane fuel cell analytical model. *Energy Conversion and Management* 164:639–54. doi:10.1016/j.enconman.2018.03.002.

Jiao, K., J. Xuan, Q. Du, Z. Bao, B. Xie, B. Wang, Y. Zhao, L. Fan, H. Wang, Z. Hou, et al. 2021. Designing the next generation of proton-exchange membrane fuel cells. *Nature*. 595(7867):361–69. doi:10.1038/s41586-021-03482-7.

Jin L, X J Wang, J W Zhu et al. 2021. Sensitivity analysis of proton exchange membrane fuel cell performance to operating parameters and its applicability assessment under different conditions. *Energy Conversion and Management* 228:113727. doi:10.1016/j.enconman.2020.113727.

Kazeminasab, B., S. Rowshanzamir, and H. Ghadamian. 2015. Multi-objective multivariable optimization of agglomerated cathode catalyst layer of a proton exchange membrane fuel cell. *Bulgarian Chemical Communications* 47:38–48.

Lin C, X Yan, G Wei et al. 2019. Optimization of configurations and cathode operating parameters on liquid-cooled proton exchange membrane fuel cell stacks by orthogonal method. *Applied Energy* 253:113496. doi:10.1016/j.apenergy.2019.113496.

Li, X., F. Tang, Q. Wang, Li, B., Dai, H., Chang, G., Zhang, C. and Ming, P. 2022. Simulation on cathode catalyst layer in proton exchange membrane fuel cell: Sensitivity of design parameters to cell performance and oxygen distribution. *International Journal of Hydrogen Energy* 47 (58):24452–63. doi:10.1016/j.ijhydene.2022.05.179.

Liu Z, X Zeng, Y Ge et al. 2017. Multi-objective optimization of operating conditions and channel structure for a proton exchange membrane fuel cell. *International Journal of Heat and Mass Transfer* 111:289–98. doi:10.1016/j.ijheatmasstransfer.2017.03.120.

Li, S., J. Yuan, G. Xie, and B. Sundén. 2018. Effects of agglomerate model parameters on transport characterization and performance of PEM fuel cells. *International Journal of Hydrogen Energy* 43 (17):8451–63. doi:10.1016/j.ijhydene.2018.03.106.

Ma X, X Zhang, J Yang et al. 2021. Impact of gas diffusion layer spatial variation properties on water management and performance of PEM fuel cells. *Energy Conversion and Management* 227:113579. doi:10.1016/j.enconman.2020.113579.

Mei, B., P. Barnoon, D. Toghraie, C. -H. Su, H. C. Nguyen, and A. Khan. 2022. Energy, exergy, environmental and economic analyzes (4E) and multi-objective optimization of a PEM fuel cell equipped with coolant channels. *Renewable and Sustainable Energy Reviews* 157:112021. doi:10.1016/j.rser.2021.112021.

Moein-Jahromi, M., and Kermani, M.J. 2021. Three-dimensional multi-phase simulation and multi-objective optimization of PEM fuel cells degradation under automotive cyclic loads. *Energy Conversion and Management* 231:113837. doi:10.1016/j.enconman.2021.113837.

Muzaffar, T., T. Kadyk, and M. Eikerling. 2018. Tipping water balance and the Pt loading effect in polymer electrolyte fuel cells: A model-based analysis. *Sustainable Energy & Fuels* 2 (6):1189–96. doi:10.1039/c8se00026c.

Nanadegani F S, E N Lay, A Iranzo et al. 2020. On neural network modeling to maximize the power output of PEMFCs. *Electrochimica acta* 348:136345. doi:10.1016/j.electacta.2020.136345.

Ogungbemi, E., T. Wilberforce, O. Ijaodola, J. Thompson, and A. G. Olabi. 2020. Review of operating condition, design parameters and material properties for proton exchange membrane fuel cells. *International Journal of Energy Research* 45 (2):1227–45. doi:10.1002/er.5810.

Xia L, S Tao , M Ni et al. 2021. Nafion degradation mechanisms in proton exchange membrane fuel cell (PEMFC) system: A review. *International Journal of Hydrogen Energy* 46 (55):27956–73. doi:10.1016/j.ijhydene.2021.06.032.

Okonkwo P C, O. Ige ,E M Barhoumi et al. 2021. Platinum degradation mechanisms in proton exchange membrane fuel cell (PEMFC) system: A review. *International Journal of Hydrogen Energy* 46 (29):15850–65. doi:10.1016/j.ijhydene.2021.02.078.

Pasaogullari, U., and Wang, C.Y. 2005. Two-phase modeling and flooding prediction of polymer electrolyte fuel cells. *Journal of the Electrochemical Society* 152 (2):A380–90. doi:10.1149/1.1850339.

Prokop, M., M. Drakselova, and K. Bouzek. 2020. Review of the experimental study and prediction of Pt-based catalyst degradation during PEM fuel cell operation. *Current Opinion in Electrochemistry* 20:20–27. doi:10.1016/j.coelec.2020.01.016.

Rivarolo, M., D. Rattazzi, T. Lamberti, and L. Magistri. 2020. Clean energy production by PEM fuel cells on tourist ships: A time-dependent analysis. *International Journal of Hydrogen Energy* 45 (47):25747–57. doi:10.1016/j.ijhydene.2019.12.086.

Secanell, M., K. Karan, A. Suleman, and N. Djilali. 2007. Multi-variable optimization of PEMFC cathodes using an agglomerate model. *Electrochimica acta* 52 (22):6318–37. doi:10.1016/j.electacta.2007.04.028.

Shahgaldi, S., A. Ozden, X. LI, and F. Hamdullahpur. 2018. Cathode catalyst layer design with gradients of ionomer distribution for proton exchange membrane fuel cells. *Energy Conversion and Management* 171:1476–86. doi:10.1016/j.enconman.2018.06.078.

Song, Y., C. Zhang, L. C. Y, M. Han, R. -Y. Yong, D. Sun, and J. Chen. 2019. Review on current research of materials, fabrication and application for bipolar plate in proton exchange membrane fuel cell. *International Journal of Hydrogen Energy* 45 (54):29832–47. doi:10.1016/j.ijhydene.2019.07.231.

Srinivasarao, M., D. Bhattacharyya, R. Rengaswamy, and Narasimhan, S. 2011. Multivariable optimization studies of cathode catalyst layer of a polymer electrolyte membrane fuel cell. *Chemical Engineering Research & Design* 89 (1):10–22. doi:10.1016/j.cherd.2010.04.020.

Stariha, S., K. Artyushkova, M. J. Workman, A. Serov, S. Mckinney, B. Halevi, and P. Atanassov. 2016. PGM-free Fe-N-C catalysts for oxygen reduction reaction: Catalyst layer design. *Journal of Power Sources* 326:43–49. doi:10.1016/j.jpowsour.2016.06.098.

Su Y,C Yin, S Huaet al. 2022. Study of cell voltage uniformity of proton exchange membrane fuel cell stack with an optimized artificial neural network model. *International Journal of Hydrogen Energy* 47 (67):29037–52. doi:10.1016/j.ijhydene.2022.06.240.

Vetter, R., and Schumacher, J.O. 2019. Free open reference implementation of a two-phase PEM fuel cell model. *Computer Physics Communications* 234:223–34. doi:10.1016/j.cpc.2018.07.023.

Wang, Y., B Seo, B Wang N. Zamel, K. Jiao, and X. C. Adroher. 2020. Fundamentals, materials, and machine learning of polymer electrolyte membrane fuel cell technology. *Energy and AI* 1:100014. doi:10.1016/j.egyai.2020.100014.

Wang, B., B Xie J. Xuan, and K. Jiao. 2020. AI-based optimization of PEM fuel cell catalyst layers for maximum power density via data-driven surrogate modeling. *Energy Conversion and Management* 205:112460. doi:10.1016/j.enconman.2019.112460.

Wang, Y., D.F.R. Diaz, K.S Chen, Z. Wang, and X. C. Adroher. 2019. Materials, technological status, and fundamentals of PEM fuel cells – a review. *Materials Today* 32:178–203. doi:10.1016/j.mattod.2019.06.005.

Wang, B., R Lin, D Liu, J Xu and Feng, B. 2019. Investigation of the effect of humidity at both electrode on the performance of PEMFC using orthogonal test method. *International Journal of Hydrogen Energy* 44 (26):13737–43. doi:10.1016/j.ijhydene.2019.03.139.

Wang, Q., F. Tang, B. Li, H. Dai, J. P. Zheng, C. Zhang, and P. Ming. 2021. Numerical analysis of static and dynamic heat transfer behaviors inside proton exchange membrane fuel cell. *Journal of Power Sources* 488:229419. doi:10.1016/j.jpowsour.2020.229419.

Wang, Y., T Liu, H Sun He, Y. Fan, and S. Wang. 2020. Investigation of dry ionomer volume fraction in cathode catalyst layer under different relative humilities and nonuniform ionomer-gradient distributions for PEM fuel cells. *Electrochimica acta* 353:136491. doi:10.1016/j.electacta.2020.136491.

Wang, B., K. Wu, Z. Yang, and K. Jiao. 2018. A quasi-2D transient model of proton exchange membrane fuel cell with anode recirculation. *Energy Conversion and Management* 171:1463–75. doi:10.1016/j.enconman.2018.06.091.

Wishart, J., Z. Dong, and M. Secanell. 2006. Optimization of a PEM fuel cell system based on empirical data and a generalized electrochemical semi-empirical model. *Journal of Power Sources* 161 (2):1041–55. doi:10.1016/j.jpowsour.2006.05.056.

Xia L, S Tao , M Ni et al., and C. Cheng. 2022. Reconstruction and optimization of catalyst layer of high temperature proton exchange membrane fuel cell. *International Journal of Hydrogen Energy* 47 (84):35778–89. doi:10.1016/j.ijhydene.2022.08.136.

Xie, B., M. Ni, G. Zhang, X. Sheng, H. Tang, Y. Xu, G. Zhai, and K. Jiao. 2022. Validation methodology for PEM fuel cell three-dimensional simulation. *International Journal of Heat and Mass Transfer* 189:122705. doi:10.1016/j.ijheatmasstransfer.2022.122705.

Xing, L., X Liu., T Alaje R. Kumar, M. Mamlouk, and K. Scott. 2014. A two-phase flow and non-isothermal agglomerate model for a proton exchange membrane (PEM) fuel cell. *Energy* 73:618–34. doi:10.1016/j.energy.2014.06.065.

Xu, Y., G. Chang, R Fan and T. Cai. 2022. Multi-objective optimization of temperature uniformity in cathode catalyst layer and performance of PEMFC with an ionomer-gradient design. *International Journal of Energy Research* 46 (15):1–17. doi:10.1002/er.8527.

Xu, Y., G. Chang, R Fan and T. Cai. 2023. Effects of various operating conditions and optimal ionomer-gradient distribution on temperature-driven water transport in cathode catalyst layer of PEMFC. *Chemical Engineering Journal* 451:138924. doi:10.1016/j.cej.2022.138924.

Xu et al., Y., G. Chang, J. Zhang, Y. Li, and S. Xu. 2021. Investigation of Inlet Gas Relative Humidity on Performance Characteristics of PEMFC Operating at Elevated Temperature. *World Electric Vehicle Journal* 12 (3):110. doi:10.3390/wevj12030110.

Yang, Y., X. Zhou, B. Li, and C. Zhang. 2021. Recent progress of the gas diffusion layer in proton exchange membrane fuel cells: Material and structure designs of microporous layer. *International Journal of Hydrogen Energy* 46 (5):4259–82. doi:10.1016/j.ijhydene.2020.10.185.

Yao J, Wu Z, Wang H et al. 2022. Design and multi-objective optimization of low-temperature proton exchange membrane fuel cells with efficient water recovery and high electrochemical performance. *Applied Energy* 324:119667. doi:10.1016/j.apenergy.2022.119667.

Zhang G, B Xie, Z Bao et al., and K. Jiao. 2018. Multi-phase simulation of proton exchange membrane fuel cell with 3D fine mesh flow field. *International Journal of Energy Research* 42 (15):4697–709. doi:10.1002/er.4215.

Zhang, G., and K. Jiao. 2018. Three-dimensional multi-phase simulation of PEMFC at high current density utilizing Eulerian-Eulerian model and two-fluid model. *Energy Conversion and Management* 176:409–21. doi:10.1016/j.enconman.2018.09.031.

Zhang, Y., A. Smirnova, A. Verma, and R. Pitchumani. 2015. Design of a proton exchange membrane (PEM) fuel cell with variable catalyst loading. *Journal of Power Sources* 291:46–57. doi:10.1016/j.jpowsour.2015.05.002.

Zhang, T., P. Wang, H. Chen, and P. Pei. 2018. A review of automotive proton exchange membrane fuel cell degradation under start-stop operating condition. *Applied Energy* 223:249–62. doi:10.1016/j.apenergy.2018.04.049.

Zhang, J., B. Wang, J Jin S. Yang, and G. Li. 2022. A review of the micro-porous layer in proton exchange membrane fuel cells: Materials and structural designs based on water transport mechanism. *Renewable and Sustainable Energy Reviews* 156:111998. doi:10.1016/j.rser.2021.111998.

Zhang, G., J. Wu, Y. Wang, Y. Yin, and K. Jiao. 2020. Investigation of current density spatial distribution in PEM fuel cells using a comprehensively validated multi-phase non-isothermal model. *International Journal of Heat and Mass Transfer* 150:119294. doi:10.1016/j.ijheatmasstransfer.2019.119294.

Zhao, J., S Cai X. Huang, X. Luo, and Z. Tu. 2021. 4E analysis and multiobjective optimization of a PEMFC-based CCHP system with dehumidification. *Energy Conversion and Management* 248:114789. doi:10.1016/j.enconman.2021.114789.

Zhao Y, Y Liu, G Liu et al. 2021. Air and hydrogen supply systems and equipment for PEM fuel cells: A review. *International Journal of Green Energy* 19 (4):331–48. doi:10.1080/15435075.2021.1946812.

Zhou, J., A. Putz, and M. Secanell. 2017. A Mixed Wettability Pore Size Distribution Based Mathematical Model for Analyzing Two-Phase Flow in Porous Electrodes. *Journal of the Electrochemical Society* 164 (6):F530–39. doi:10.1149/2.0381706jes.